

# Formation of Spontaneous Density-Wave Patterns in dc Driven Lattices

H. P. Zahn,<sup>1</sup> V. P. Singh<sup>2,3</sup>, M. N. Kosch,<sup>1</sup> L. Asteria<sup>2</sup>, L. Freystatzky,<sup>2,4</sup> K. Sengstock,<sup>1,2,4</sup>  
L. Mathey,<sup>1,2,4</sup> and C. Weitenberg<sup>1,4,\*</sup>

<sup>1</sup>*Institut für Laserphysik, Universität Hamburg, 22761 Hamburg, Germany*

<sup>2</sup>*Zentrum für Optische Quantentechnologien, Universität Hamburg, 22761 Hamburg, Germany*

<sup>3</sup>*Institut für Theoretische Physik, Leibniz Universität Hannover, 30167 Hannover, Germany*

<sup>4</sup>*The Hamburg Centre for Ultrafast Imaging, 22761 Hamburg, Germany*



(Received 15 November 2021; accepted 24 February 2022; published 19 April 2022)

Driving a many-body system out of equilibrium induces phenomena such as the emergence and decay of transient states, which can manifest itself as pattern and domain formation. The understanding of these phenomena expands the scope of established thermodynamics into the out-of-equilibrium domain. Here, we experimentally and theoretically study the out-of-equilibrium dynamics of a bosonic lattice model subjected to a strong dc field, realized as ultracold atoms in a strongly tilted triangular optical lattice. We observe the emergence of pronounced density-wave patterns—which spontaneously break the underlying lattice symmetry—using a novel single-shot imaging technique with two-dimensional single-site resolution in three-dimensional systems, which also resolves the domain structure. Our study suggests that the short-time dynamics arises from resonant pair tunneling processes within an effective description of the tilted Hubbard model. More broadly, we establish the far out-of-equilibrium regime of lattice models subjected to a strong dc field, as an exemplary and paradigmatic scenario for transient pattern formation.

DOI: [10.1103/PhysRevX.12.021014](https://doi.org/10.1103/PhysRevX.12.021014)

Subject Areas: Atomic and Molecular Physics  
Nonlinear Dynamics, Quantum Physics

## I. INTRODUCTION

The appearance of patterns, which spontaneously break the spatial symmetry of the underlying potential landscapes, belongs to the most fascinating aspects in physics. Famous examples range from sand dune ripples to soliton trains in shallow water, where macroscopic patterns appear in driven systems on a homogeneous background landscape with continuous symmetry [1]. Such phenomena can be probed in the quantum regime using ultracold atoms, where pattern formation arises, e.g., due to periodic driving [2] or due to long-range interactions as supersolid stripe pattern [3]. Of special interest are periodic potentials, in which density waves or spin waves can spontaneously break the underlying lattice symmetry in a discrete fashion as observed, e.g., for tilted Bose-Hubbard models [4–8] or for spin chains formed by Rydberg-atom arrays [9].

Here we observe the formation of a pronounced density wave for a Bose-Einstein condensate in a two-dimensional triangular lattice of tubes after applying a strong tilt, i.e., a spatially periodic modulation of the lattice occupations.

The observed density wave can be attributed to the resonant pair tunneling and nearest-neighbor interaction terms that emerge as dominant terms in the effective Hamiltonian of the dc driven system and it appears on a timescale of  $\sim 30$  ms. At later times, the interplay of the direct tunneling and the emergent terms leads to an intriguing open-system dynamics, where the density-wave period increases. While density waves can appear as ground states for extended Hubbard models [10], the ground state for our parameters has no density wave and the observed pattern formation occurs far from equilibrium after the quench into the tilted system. For a conceptual understanding of the early-time dynamics, we derive the effective Hamiltonian for bosons on the strongly tilted triangular lattice and use a  $c$ -field simulation to confirm both the experimental observations and the scalings of the effective Hamiltonian.

We employ a novel microscopy technique [11] (Appendix C) as an indispensable tool to directly image the density-wave order and its domains in the 2D lattice of tubes with single-site resolution. This microscopy directly reveals the spontaneous symmetry breaking in the pattern formation and domains thereof. Our striking observation of spontaneous pattern formation is very distinct from recent experiments in tilted optical lattices in the regime of unit occupation [12,13], where a suppressed decay of initially prepared density waves due to Stark many-body localization or kinetic constraints, but no pattern formation, was observed. In contrast, occupation of period-doubled states

\*christof.weitenberg@physnet.uni-hamburg.de

Published by the American Physical Society under the terms of the [Creative Commons Attribution 4.0 International license](https://creativecommons.org/licenses/by/4.0/). Further distribution of this work must maintain attribution to the author(s) and the published article's title, journal citation, and DOI.

was previously inferred from momentum-space images in the regime of large bosonic filling factors in an array of tubes, similar to our system that we resolve in real space with the novel microscopy technique. However, this pattern formation was triggered by the different mechanism of dynamical instability in fully coherent systems, which occurs both in moving lattices [14,15] and in periodically driven lattices [16].

## II. EXPERIMENTAL SETUP

Our experiments start with a Bose-Einstein condensate (BEC) of  $\sim 5 \times 10^4$   $^{87}\text{Rb}$  atoms in a triangular optical lattice with tunnel coupling  $J = h \times 13$  Hz and transverse confinement  $\omega_z = 2\pi \times 30$  Hz, for which we estimate an equivalent Hubbard interaction term  $U \sim h \times 2.3$  Hz [Fig. 1(a)]. The lattice laser wavelength is  $\lambda = 1064$  nm yielding a lattice constant  $a = 2\lambda/3$  and a distance between lattice sites in the tilt direction of  $\tilde{a} = a\sqrt{3}/2$ . We apply a tilt by shifting the magnetic trap, let the system evolve, and image the real-space distribution with the quantum gas magnifier [11], i.e., by magnifying the distribution using matter-wave optics prior to optical imaging. The shift of the trap is realized by switching off a magnetic offset field on the timescale of few tens of microseconds, i.e., much faster than all other timescales including the tunneling time, and we therefore consider this quench instantaneous in the analysis. Note that this protocol leads to a nonuniform tilt due to the curvature of the trap (Appendix C). While such a nonuniformity was found to have profound effects in the regime of many-body localization [17,18], we do not find significant effects in our regime of large bosonic occupations when comparing to a system with homogeneous tilt in numerical simulations (Appendix A).

We identify the relevant regime of tilts, where the atoms are Stark localized and form a metastable system on the slope of the potential [19,20], while still showing sufficiently strong pair tunneling driving the density-wave formation. We work at a tilt of  $F = h \times 2.3$  kHz/ $\mu\text{m}$ , which leads to an energy offset between neighboring lattice sites of  $\Delta = F\tilde{a} = h \times 1.4$  kHz and to a large suppression of tunneling  $J/\Delta = 0.009$ . The resulting density distributions are presented in Fig. 1(d) and show the pronounced density waves with random phase constituting spontaneous symmetry breaking, as we discuss below. We model the system with extensive *c*-field simulations (Appendix A) and find qualitative agreement when comparing the site occupations [Fig. 1(e)], as also discussed below.

## III. THEORETICAL MODELING

To describe the system, we introduce an effective Hamiltonian (Appendix B): the energy offset  $\Delta$  introduces a relative phase evolution, which can be treated in a Floquet picture yielding an effective Hamiltonian  $\hat{H}_{\text{eff}}$  in a high-frequency approximation.  $\hat{H}_{\text{eff}}$  contains new processes with

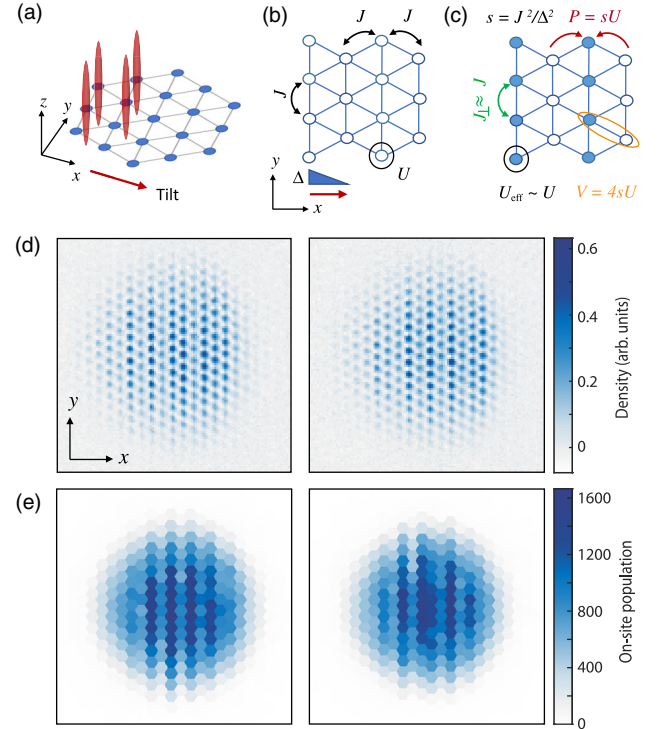


FIG. 1. Bose-Einstein condensates in strongly tilted optical lattices. (a) The system consists of a triangular lattice of tubes with a tilt applied perpendicularly to a lattice vector. (b) The system can be described by a Hubbard model with tunnel coupling  $J$ , on-site interaction  $U$ , and energy offset  $\Delta$  along the tilt direction. (c) In the large tilt limit the system can be described by an effective Hamiltonian with no tilt and no single-particle tunneling in the tilt direction, but pair tunneling  $P$  and nearest-neighbor interaction  $V$  with a strength set by  $sU$  with  $s = (J/\Delta)^2$ . Tunneling perpendicular to the tilt  $J_{\perp}$  and the effective on-site interaction  $U_{\text{eff}}$  remain approximately unchanged. (d) Experimental images of the spatial density show the spontaneous formation of charge density waves with wave vector parallel to the tilt direction. The two example images are for identical parameters of a hold time of 60 ms and tilt with energy offset  $\Delta = h \times 1.4$  kHz, but one shows a domain wall in the center of the cloud and the other does not, directly reflecting the spontaneous nature of the pattern. The tunnel coupling is  $J = h \times 13$  Hz throughout the paper. (e) *c*-field simulation for the same parameters as in (d). The simulation does not model the density modulation within the lattice sites and the density distribution is therefore shown as tiled hexagons.

a scale  $s = (J/\Delta)^2$ : a center-of-mass-conserving pair tunneling, where one atom goes up the tilt and the other goes down, with strength  $P = sU$ , and a next neighbor interaction with strength  $V = 4sU$  [Figs. 1(b) and 1(c)]. These processes are dominant, because the direct tunneling  $J$  along the tilt is suppressed and vanishes in  $\hat{H}_{\text{eff}}$ . The choice of the triangular lattice enhances the pair tunneling dynamics, because each lattice site has two neighbors on top and below, which gives rise to four possible pair tunneling terms. To motivate why the pair tunneling terms

give rise to the density-wave pattern in the quench dynamics, we evaluate the density correlation function averaged over all states that are connected to an initial homogeneous state via a finite number of pair tunneling processes and find the staggered correlations indicative of the density wave (Appendix B).

The effective Hamiltonian features a density wave as ground state in a regime of larger  $P$  and  $V$  (see Monte Carlo studies in Appendix B), whereas here, interestingly, the density wave appears as a transient nonequilibrium phenomenon after the quench, and for this dynamics, the pair tunneling  $P$  sets the relevant scale. This observation also suggests an interpretation as a prethermalized state [21] of the time evolution triggered by the quench, in which the system does not directly relax to a thermal state of either the underlying or the effective Hamiltonian, but rather relaxes in a two-step process via a density-ordered state.

#### IV. SPONTANEOUS SYMMETRY BREAKING

The density wave has twice the period of the underlying lattice and can therefore spontaneously choose between two positions, giving rise to a discrete symmetry breaking. We quantify this by a density-wave order of positive or negative sign, depending on whether the density wave is in or out of phase with a globally fixed reference pattern. This is realized by multiplying the residues with this reference pattern of alternating positive and negative sign [Fig. 2(a)]. We find that this density-wave order forms large domains of a random sign of the order [Fig. 2(b)], demonstrating the spontaneous nature of the symmetry breaking. The double-peak structure of a histogram of the local density-wave order values reflects the spontaneous symmetry breaking as well [Fig. 2(c)]. This is further supported by the persistence of the double-peak structure after postselection on the position of the lattice relative to the initial cloud center (Appendix E), which is not triggering the symmetry breaking. For longer hold times we observe a pinning of the density wave, which we discuss in Appendix E.

#### V. EMERGENCE AND DECAY OF DENSITY-WAVE ORDER

Moving further, we study the intriguing dynamics of the density-wave order, which is characterized by a spontaneous emergence and a very long-lived decay. First, we quantify the period of the density-wave pattern via the power spectral density (PSD)  $|n_k|^2 = |(\mathcal{F}n_x)(k)|^2/N_{\text{tot}}^2$  of the column populations  $n_x$  normalized by the total atom number  $N_{\text{tot}}$ , which captures the spectrum of the density-density correlations [Fig. 3(a)]: we find an initial peak at  $k\tilde{a}/(2\pi) = \pm 1/2$  (period 2), which splits and moves to  $k\tilde{a}/(2\pi) \sim \pm 1/3$  (period 3) at longer times when the single-particle tunneling starts a transport down the slope.

We define the density-wave contrast as the relative integrated PSD in this peak:

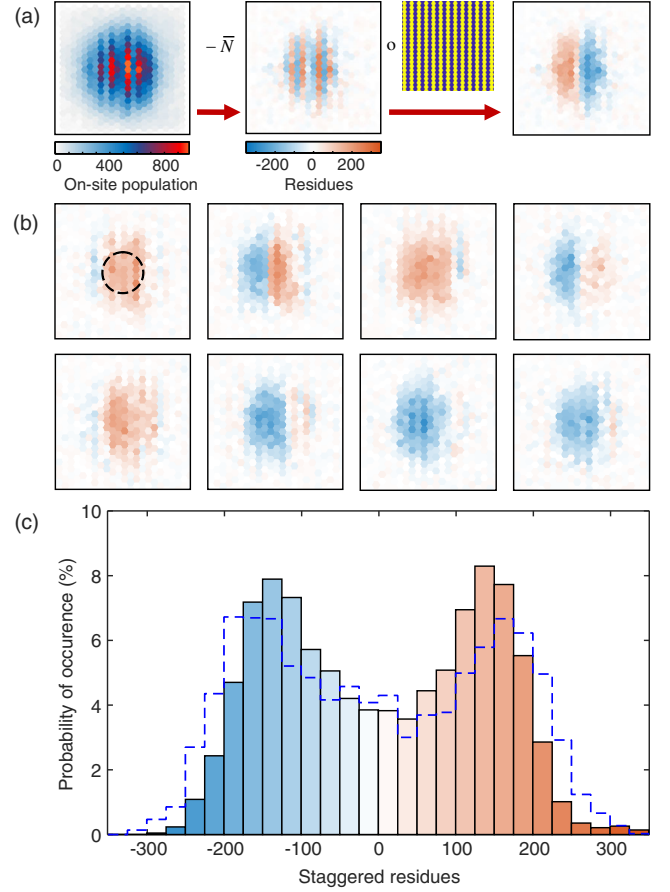


FIG. 2. Spontaneous symmetry breaking. (a) The local density-wave order is quantified by calculating the residues after subtracting the mean density of about 130 identically prepared clouds. Multiplying by a staggering of fixed phase yields the staggered residues, which act as domain identifier. (b) Staggered residues for typical individual images with  $\Delta = h \times 1.4$  kHz energy offset and 60 ms hold time illustrating the spontaneous formation of domains in the density-wave order with typically one or two large domains. (c) Histogram of the staggered residues for all lattice sites within a region of interest [dashed circle of radius 3 sites in (b)]. The dashed line represents the histogram for a numerical simulation with  $k_B T/J = 250$  and a peak density of 900 atoms per tube.

$$c = \int_{1/5}^{1/2} |n_k|^2 d(k\tilde{a}/2\pi) / \int_0^{1/2} |n_k|^2 d(k\tilde{a}/2\pi). \quad (1)$$

This signal appears within  $\sim 30$  ms, reaches a maximum at around  $\sim 200$  ms, and then shows almost no sign of decay for over 1.6 s [Fig. 3(b)]. The long lifetime is captured well by a  $c$ -field simulation, when the atom number loss of the experiment is added to the simulation (Appendixes A and C). This behavior points to the interaction-driven nature of the density-wave dynamics, which is frozen when the density drops (Appendix F).

Concerning the structure of the patterns there are differences between the experiment and the simulations

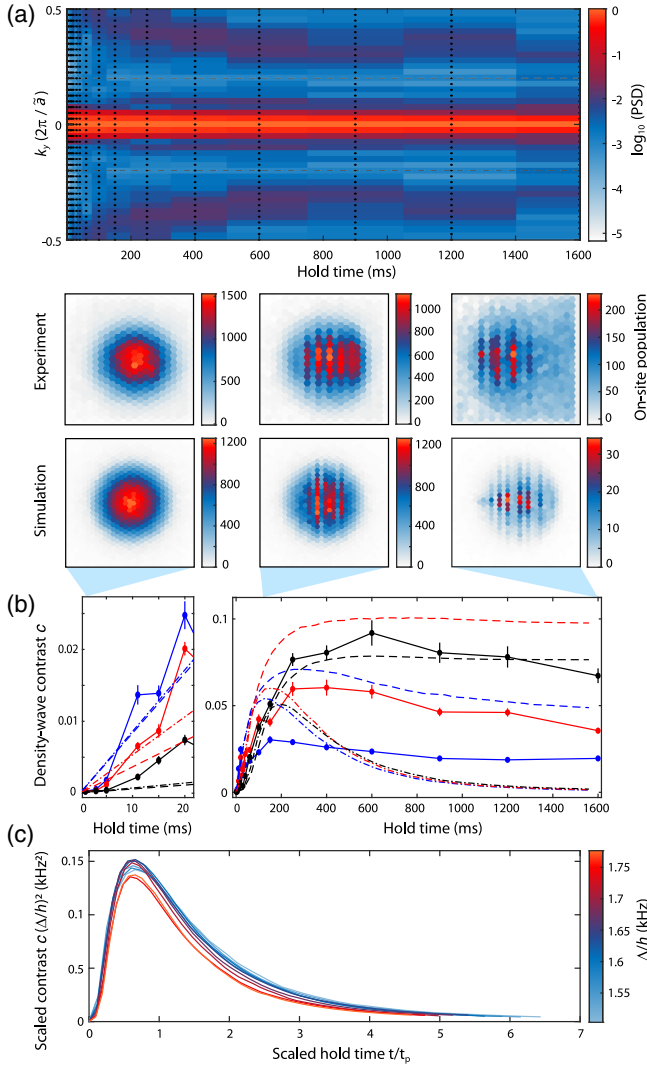


FIG. 3. Formation dynamics and decay of the density wave. (a) The normalized power spectral density of the column occupations for a tilt with energy offset  $\Delta = h \times 1.4$  kHz initially develops a peak at  $k\bar{a}/(2\pi) = \pm 1/2$  (period 2), which splits and moves to  $k\bar{a}/(2\pi) \sim \pm 1/3$  (period 3) at longer time. The dots show the exact parameters for which data were taken. The dashed lines mark  $k\bar{a}/(2\pi) = \pm 1/5$ , which is used in the computation of the density-wave contrast (see main text). (b) Dynamics of the density-wave contrast  $c$  for different evolution times after the quench into the tilted system showing the fast buildup and slow decay of the patterns. The color encodes the tilt strength of  $\Delta = h \times 1.1$  kHz (blue),  $\Delta = h \times 1.4$  kHz (red),  $\Delta = h \times 1.7$  kHz (black). The experimental data (circles) are compared to a numerical  $c$ -field simulation including the atom number loss (dashed lines) and without loss (dash-dotted lines). The numerical simulation without atom loss shows a faster decay. The simulation uses a temperature of  $k_B T/J = 100$ . The insets show example single-shot density distributions from the experiment (top row, hold time is 1, 60, and 1600 ms) and the simulation with atom loss (bottom row, hold time is 0, 64, and 1560 ms). All error bars correspond to the 68% confidence interval. (c) The density-wave order of the simulated data without atom loss follows the scaling of the effective Hamiltonian and collapses on a curve when the time axis is rescaled by the pair tunneling time  $t_p$  and the density-wave order is scaled by the energy offset squared  $\Delta^2$ .

at long times: the evolution toward period 3 patterns for these times [Fig. 3(a)] is not quantitatively reproduced by the simulation, where this change is less pronounced. This intriguing dynamics remains to be explained. The difference between experiment and simulation might be due to occupations of higher bands after the quench, which are not included in the simulation. Note that in our finite system, an interpretation of a period 3 pattern cannot be clearly distinguished from a period 2 pattern with several domain walls. This motivates the analysis via the period-independent measure of the density-wave contrast defined above.

For the understanding of the dynamics, it is instructive to refer to the effective Hamiltonian introduced above. It defines a timescale (Appendix B)  $t_p = h/(16NP) \approx 210$  ms for the density-wave formation dynamics, where we used  $\Delta = h \times 1.4$  kHz and where  $N \approx 1500$  is the number of atoms in the central tube for the data in Fig. 3. The scaling  $t_p \propto \Delta^2$  fits well with the density-wave dynamics in the  $c$ -field simulation without atom number loss [Fig. 3(c)], which therefore confirms this Floquet picture. The dependence of  $t_p$  on  $N$  explains why the dynamics is frozen with atom loss leading to long-lived density-wave patterns and why the simulation needs to include the atom number loss to reproduce the slow decay. We also study the influence of coherence between the lattice sites by realizing different temperatures and find that initial coherence is required for the formation of the density wave (Appendix F).

## VI. EFFECT OF TRANSVERSE TUNNELING

In another set of experiments we study the effect of transverse tunneling, i.e., tunneling perpendicular to the tilt. We compare the situation of two different tilt directions, which have equal tight-binding models except for a very different strength of the transverse tunneling within the triangular lattice [Figs. 4(a) and 4(b)]. The resulting images reveal that the density-wave pattern becomes more irregular without the transverse tunneling [Figs. 4(c) and 4(d)], which is directly reflected in the density correlations [Figs. 4(e) and 4(f)]. In both cases, we find staggered density correlations of the density-wave order along the tilt and monotonically decaying correlations perpendicular to the tilt, but with different ranges [Figs. 4(g) and 4(h)]. We heuristically fit the decay and state the decay lengths  $L_\perp$  and  $L_\parallel$  in units of the number of lattice sites (Appendix D). Interestingly, the range of the staggered density-wave order along the tilt has the same decay length  $L_\parallel$  of 2.1(7) and 2.3(5) sites for the strong and weak transverse tunneling, respectively. The correlation length perpendicular to the tilt  $L_\perp$ , however, is drastically reduced from long-range order to short-range order with decay length  $L_\perp$  of 1.2(3) sites when changing the tilt direction. The analysis shows that strong transverse tunneling aligns the phase of the

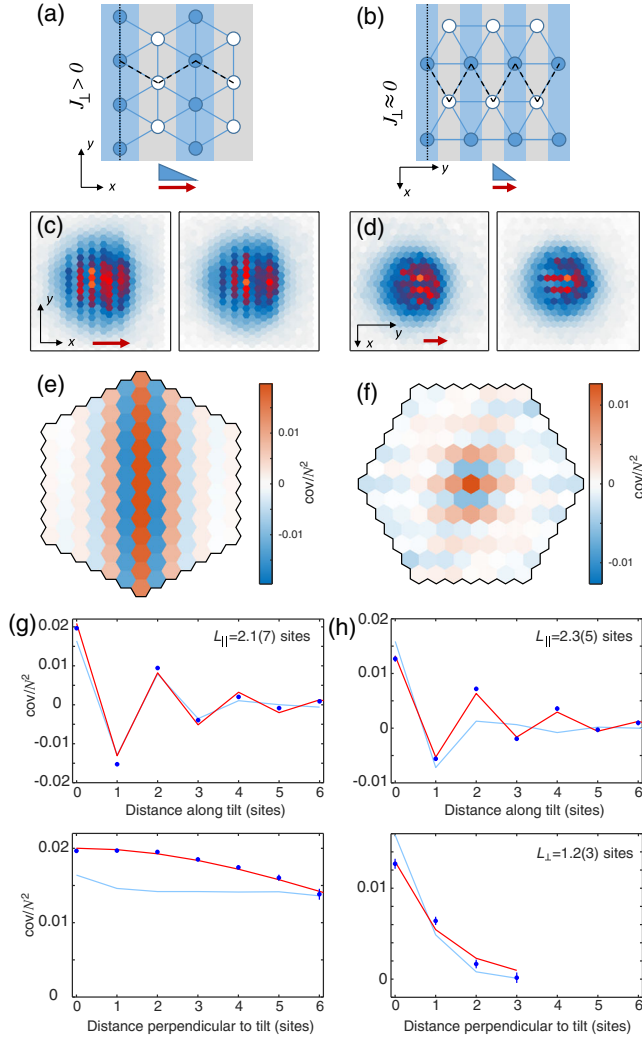


FIG. 4. Dependence on the tilt direction. (a) Sketch of the triangular lattice geometry and the columns (gray and blue bars) perpendicular to the tilt for the two situations with different values of transverse tunneling  $J_{\perp}$ . (b) Sketch of the situation with the tilt in the perpendicular direction. Here tunneling within the columns only appears as a higher-order process. For an easier comparison, we have rotated the system, such that the tilt always points to the right. (c), (d) Typical experimental images for the two tilt directions with energy offset  $\Delta = h \times 1.4$  kHz, a hold time of 60 ms, and a maximum atom number per tube of 900 and 850, respectively. The orientation of the images and the tilt direction (red arrow) are as in (a) and (b), respectively. (e), (f) The density correlation functions (Appendix D) for the two cases. (g), (h) Cuts of the density correlation functions show the density-wave order measured along a zigzag path along the tilt direction [dashed line in (a) and (b)] and a monotonic decay within the columns [dotted line in (a) and (b)]. The red lines show heuristic fits (Appendix D) to the data, the light blue lines result from the same analysis on pictures from numerical simulations with  $k_B T / J = 50$ . All error bars correspond to the 68% confidence interval. Note that while (d) and (f) give the visual impression of horizontal stripes, they should be thought of as vertical stripes [as sketched by the blue and gray coloring in (b)]. This is because the horizontal bonds (which would connect the supposed horizontal stripes) are suppressed by  $2\Delta$  in the effective model.

symmetry breaking density waves across the system while the range of the staggered order along the tilt is not affected.

## VII. CONCLUSION

In conclusion, we have observed the appearance of long-lived density-wave patterns for a BEC in a strongly tilted two-dimensional optical lattice and confirmed their spontaneous breaking of the discrete lattice symmetry. The dynamics is supported by a Floquet picture, which introduces correlated pair tunneling processes and sets the density-dependent timescale. The findings continuously connect to the charge density wave observed in a tilted bosonic Mott insulator in the unit-filling regime [4–6,8], with its mapping to quantum spin models. By going away from solvable models toward full-fledged high-dimensional many-body systems, we identify an intriguing regime of many-body dynamics.

With these experiments we establish the quantum gas magnifier for imaging spontaneously formed pattern on the scale of single lattice sites in 3D systems. The technique can in principle also image the coherence properties with high resolution [11], and in the future it could be used to observe other exotic states such as the twisted superfluid [22] or to resolve domains of spontaneous symmetry breaking of phase patterns in driven lattices [23,24] and in higher bands [25]. With the observation of spatial symmetry breaking in a nonequilibrium situation, we set the stage for observing density-wave ground states by engineering stronger nonstandard Hubbard terms [26,27].

The description of the observed dynamics by the terms of a Floquet picture points a way to use dc driven systems [28–30] as opposed to ac driven systems for Floquet engineering of relevant extended Hubbard models [31]. While for ac driven Floquet systems many-body localization has been proposed for stabilization against heating, dc driven systems require Stark localization (and potentially many-body Stark localization [17]) for stabilization and our experiments show that it is promising to identify suitable regimes. Of particular interest would be extended Hubbard models in the strongly correlated regime featuring exotic states such as topological Mott insulators [32] or other density-assisted tunneling terms for engineering artificial magnetic fields [33]. Furthermore, the dc drive could be combined with an ac drive leading to rich phenomena such as topological band gap solitons [34] or Stark time crystals [35].

## ACKNOWLEDGMENTS

The work is funded by the Cluster of Excellence “CUI: Advanced Imaging of Matter” of the Deutsche Forschungsgemeinschaft (DFG)—EXC 2056—Project No. 390715994, by the DFG Collaborative Research Center SFB 925, Project No. 170620586, and by the DFG Research Unit FOR 2414, Project No. 277974659. C.W. acknowledges funding by the European Research

Council (ERC) under the European Union’s Horizon 2020 research and innovation programme under Grant Agreement No. 802701. V. P. S. acknowledges funding by the Cluster of Excellence “QuantumFrontiers”—EXC 2123—Project No. 390837967.

## APPENDIX A: NUMERICAL SIMULATION OF THE EXPERIMENT

### 1. *c*-field simulation

We simulate the dynamics of tube condensates arranged in a 2D triangular geometry using the classical-field method of Ref. [36]. The system is described by the Bose-Hubbard model,

$$\hat{H} = -\sum_{\langle ij \rangle} J_{ij}(\hat{\psi}_i^\dagger \hat{\psi}_j + \hat{\psi}_i \hat{\psi}_j^\dagger) + \frac{\tilde{U}}{2} \sum_i \hat{n}_i^2 + \sum_i V_i \hat{n}_i, \quad (\text{A1})$$

where  $\hat{\psi}_i$  ( $\hat{\psi}_i^\dagger$ ) is the bosonic annihilation (creation) operator and  $\hat{n}_i = \hat{\psi}_i^\dagger \hat{\psi}_i$  is the occupation operator at site  $i$ .  $\langle ij \rangle$  denotes nearest-neighbor bonds and  $J_{ij}$  are the corresponding tunneling energies.  $\tilde{U}$  is the on-site interaction energy and  $V_i$  is the harmonic trap potential. The lattice site locations  $\mathbf{r}_i = (x_i, y_i, z)$  represent a 3D system, which is continuous in the  $z$  direction. We choose the primitive vectors  $\mathbf{a}_1 = a\mathbf{e}_y$  and  $\mathbf{a}_2 = \sqrt{3}/2\mathbf{e}_x + 1/2\mathbf{e}_y$  resulting in  $\mathbf{r}_i = i_1\mathbf{a}_1 + i_2\mathbf{a}_2 + z\mathbf{e}_z$ , with  $a = 709$  nm being the lattice constant. We have the same tunneling energy  $J = h \times 13$  Hz for all 6 neighbors. The 3D repulsive interaction is determined by  $g_{3D} = \hbar^2 a_s / (\pi m)$ , where  $a_s$  is the  $s$ -wave scattering length and  $m$  is the atomic mass. For the tubes, this results in an effective 1D interaction  $g_{1D} = g_{3D} / (2\pi a_{\text{osc}}^2)$ , with  $a_{\text{osc}}$  being the oscillator length determined by the lattice depth and the recoil energy. Using the experimental parameters we obtain  $g_{1D} = 7.06J \mu\text{m}$ . For numerical simulations we discretize the  $z$  direction with a discretization length of  $\ell_z = 0.4 \mu\text{m}$ . This introduces an additional effective coupling in  $z$  direction,  $J_z = \hbar^2 / (8\pi^2 m \ell_z^2) = 27.9J$ , and the on-site interaction is rescaled to  $U_{\text{site}} = g_{1D} / \ell_z = 17.6J$  (Refs. [23,37]). We use the same trap frequencies  $\omega_{x,y} = 2\pi \times 135$  Hz and  $\omega_z = 2\pi \times 30$  Hz as in the experiments. The atom number of the central tube is chosen according to the experimental values. The temperature is more difficult to determine in the experiment and the temperature in the numerics is chosen to match the experimental results as stated in the respective captions (Figs. 2–4, 12, and 13).

We simulate this system using a numerical lattice of size  $N_x \times N_y \times N_z$ , where  $N_x$  and  $N_y$  are chosen between 50 and 100 and  $N_z$  is fixed at  $N_z = 81$ . In our *c*-field representation we replace the operators  $\hat{\psi}$  in Eq. (A1) and in the equations of motion by complex numbers  $\psi$ . We sample the initial states in a grand-canonical ensemble of temperature  $T$  and chemical potential  $\mu$  via a classical Metropolis algorithm. We then propagate each state using

the classical equations of motion. We calculate the observable such as the tube density  $n(x, y, t)$  and average over the initial ensemble. For tilting the system, we adopt the experimental procedure and therefore abruptly displace the harmonic trap by a displacement  $d$  either along the lattice direction or perpendicular to the lattice direction. To implement atom loss, we additionally include the term  $-\gamma n_i$  in the equations of motion, where  $\gamma$  is the loss rate. We use the experimentally determined  $\gamma$  from the time evolution of density up to 100 ms (see Appendix C). We note that the measured  $\gamma$  varies depending on the value of  $d$ .

### 2. Derivation of the Hubbard interaction strength

We estimate an effective Hubbard interaction strength  $U$  using the ansatz for the wave function in a single lattice site  $\varphi(x, y, z) = \varphi_{2D}(x, y)\varphi_z(z)$ , where  $\varphi_{2D}(x, y)$  is the wave function in the lattice plane and it is determined by the lattice depth, and  $\varphi_z(z)$  is the wave function in  $z$  direction which we assume to be a Thomas-Fermi profile. We determine  $\varphi(x, y, z)$  for  $N = 1000$  atoms and extract the total interaction energy as  $E_{\text{int}} = N^2 g_{3D} \int |\varphi(x, y, z)|^4 dx dy dz$ . We obtain an effective Hubbard strength  $U = (2/N^2)E_{\text{int}}$  of  $\sim h \times 2.3$  Hz. This derivation neglects the change of the Thomas-Fermi profile with the atom number per tube, which is valid for small relative atom number changes during the initial dynamics. This effective Hubbard  $U$  is only used for the computation of  $t_p$  via the effective Hamiltonian, but not for the description via the *c*-field simulation, where a different Hubbard  $U_{\text{site}}$  appears for the description with discretized  $z$  direction.

### 3. Simulations with homogeneous tilt

In order to investigate the role of the inhomogeneity of the tilt due to the curvature of the magnetic trap, we perform *c*-field simulations with a homogeneous tilt with hard walls to keep the system finite. We use an energy

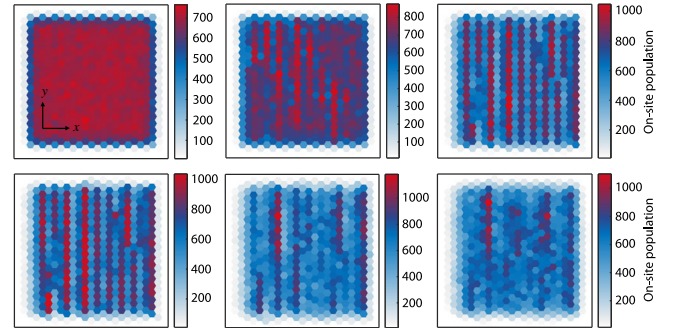


FIG. 5. Simulation of a homogeneously tilted lattice. Time series of the on-site populations for a BEC in a lattice with hard wall boundary conditions homogeneously tilted along the  $x$  direction. The hold times after initialization are 0, 10, 60, 100, 300, and 600 ms, from left to right and top to bottom. The dynamics are similar to that of the inhomogeneous system studied in the main text [Fig. 3(a)].

offset of  $\Delta = 1.3$  kHz, a tunneling energy of  $J = 10$  Hz, a temperature of  $k_B T/J = 100$ ,  $N = 700$  atoms per tube, and keep the value of  $\tilde{U}$  as in the main text. The density-wave pattern forms in a similar manner compared to the situation with inhomogeneity (Fig. 5). We do not include any atom loss, which is why the density-wave contrast decays at long times as in the inhomogeneous system.

## APPENDIX B: EFFECTIVE HAMILTONIAN PICTURE

### 1. Derivation of the effective Hamiltonian

We describe the 2D triangular lattice by the Bose-Hubbard Hamiltonian,

$$\hat{H}_0 = -J \sum_{\langle jk \rangle} (\hat{b}_j^\dagger \hat{b}_k + \hat{b}_k^\dagger \hat{b}_j) + \frac{U}{2} \sum_j \hat{n}_j (\hat{n}_j - 1), \quad (\text{B1})$$

where  $\hat{b}_j$  is the bosonic annihilation operator and  $\hat{n}_j = \hat{b}_j^\dagger \hat{b}_j$  is the number operator at site  $j$ .  $\langle jk \rangle$  denotes nearest neighbors. We add the lattice tilt perpendicular to a primitive lattice vector by the term  $\hat{H}_\Delta = \Delta \sum_j x_j \hat{n}_j$ , where  $x_j$  is the  $x$  coordinate of site  $j$ . The tilt energy  $\Delta$  is the dominant energy scale, since  $\Delta \gg J, U$ . To include the effect of the tilt in the system, we go to the interaction picture with respect to  $\hat{H}_\Delta$  and obtain

$$\hat{H}_I = \exp(i\hat{H}_\Delta t) \hat{H}_0 \exp(-i\hat{H}_\Delta t), \quad (\text{B2})$$

$$\hat{b}_j(t) = \exp(i\hat{H}_\Delta t) \hat{b}_j \exp(-i\hat{H}_\Delta t) = \hat{b}_j \exp(-ix_j \Delta t), \quad (\text{B3})$$

$$\hat{b}_j^\dagger(t) = \exp(i\hat{H}_\Delta t) \hat{b}_j^\dagger \exp(-i\hat{H}_\Delta t) = \hat{b}_j^\dagger \exp(ix_j \Delta t). \quad (\text{B4})$$

This results in

$$\hat{H}_I = \hat{H}_U + \hat{H}_J + \hat{H}_1 \exp(-i\Delta t) + \hat{H}_{-1} \exp(i\Delta t), \quad (\text{B5})$$

with

$$\hat{H}_U = \frac{U}{2} \sum_j \hat{n}_j (\hat{n}_j - 1), \quad (\text{B6})$$

$$\hat{H}_J = -J \sum_{\langle jk \rangle_y} \left( \hat{b}_j^\dagger \hat{b}_k + \hat{b}_k^\dagger \hat{b}_j \right), \quad (\text{B7})$$

$$\hat{H}_1 = -J \sum_{\langle jk \rangle_{x+}} \hat{b}_j^\dagger \hat{b}_k, \quad (\text{B8})$$

$$\hat{H}_{-1} = -J \sum_{\langle jk \rangle_{x-}} \hat{b}_j^\dagger \hat{b}_k. \quad (\text{B9})$$

$\langle jk \rangle_y$  denotes nearest neighbors in the  $y$  direction,  $\langle jk \rangle_{x\pm}$  are the nearest neighbors in  $x$  directions such that the tilt potential on site  $k$  is bigger (smaller) than at site  $j$ .

Equation (B5) is the form of a periodically driven system with frequency  $\Delta$ , which allows us to use a Magnus expansion [38–40]. We consider Magnus expansion to second order:

$$\begin{aligned} \hat{H}_{\text{eff}}^{(2,2)} = & -\frac{1}{2\Delta^2} [[\hat{H}_U + \hat{H}_J, \hat{H}_1], \hat{H}_{-1}] \\ & -\frac{1}{2\Delta^2} [[\hat{H}_U + \hat{H}_J, \hat{H}_{-1}], \hat{H}_1]. \end{aligned} \quad (\text{B10})$$

We note that the first-order term vanishes in the expansion. We solve the double commutators and obtain the effective Hamiltonian:

$$\hat{H}_{\text{eff}} = \hat{H}_U + \hat{H}_J + \hat{H}_{\text{eff}}^{(2,2)} \quad (\text{B11})$$

$$\equiv \hat{H}_{U,\text{eff}} + \hat{H}_{J_\perp} + \hat{H}_P, \quad (\text{B12})$$

where

$$\hat{H}_{U,\text{eff}} = \left( \frac{U}{2} - 4sU \right) \sum_j \hat{n}_j (\hat{n}_j - 1) + 4sU \sum_{\langle jk \rangle_y} \hat{n}_j \hat{n}_k, \quad (\text{B13})$$

$$\hat{H}_P = -sU \sum_{\langle jkl \rangle_x} \left( \hat{b}_j^\dagger \hat{b}_j^\dagger \hat{b}_k \hat{b}_l + \hat{b}_l^\dagger \hat{b}_k^\dagger \hat{b}_j \hat{b}_j \right), \quad (\text{B14})$$

$$\begin{aligned} \hat{H}_{J_\perp} = & -\sum_{\langle jk \rangle_y} (J \hat{b}_j^\dagger \hat{b}_k + sU \hat{b}_j^\dagger \hat{n}_j \hat{b}_k + sU \hat{b}_j^\dagger \hat{n}_k \hat{b}_k + \text{H.c.}) \\ & + 2sU \sum_{\langle jkl \rangle_\Delta} (\hat{b}_j^\dagger \hat{n}_l \hat{b}_k + \hat{b}_k^\dagger \hat{n}_l \hat{b}_j). \end{aligned} \quad (\text{B15})$$

$\langle jk \rangle_{x(y)}$  denotes nearest neighbors in the  $x(y)$  direction,  $\langle jkl \rangle_x$  are all pairs of bonds with one bond up and one down the tilt, and  $\langle jkl \rangle_\Delta$  denotes triangular plaquettes such that  $j$  and  $k$  are nearest neighbors in the  $y$  direction.

Compared to the original model, most lattice parameters are slightly renormalized by the tilt. The interaction scales as  $U \rightarrow U - 8sU$ . The hopping transverse to the tilt scales as  $J_\perp \rightarrow J - 2sUn$ , where this correction comes from second-order tunneling processes and  $n$  is the mean-field density. The single-particle hopping along the tilt does not appear in the effective Hamiltonian. In  $\hat{H}_{U,\text{eff}}$  and  $\hat{H}_P$ , the new terms are nearest-neighbor repulsion and pair hopping. The second term in Eq. (B15) is a density induced tunneling term, which appears transverse to the tilt [41].

For a tilt along one lattice vector [Figs. 6(b) and 6(d)] the general idea stays the same. In this case Eq. (B5) contains additional terms with  $\exp(\pm 2i\Delta t)$  and therefore additional terms appear in the effective Hamiltonian. On the other hand, the direct hopping perpendicular to the tilt does not exist and coherence in this direction can only be built by second-order processes. To describe the effective Hamiltonian for this case, we define the tilt energy offset  $\Delta$  as indicated in Fig. 6. We obtain the effective Hamiltonian,

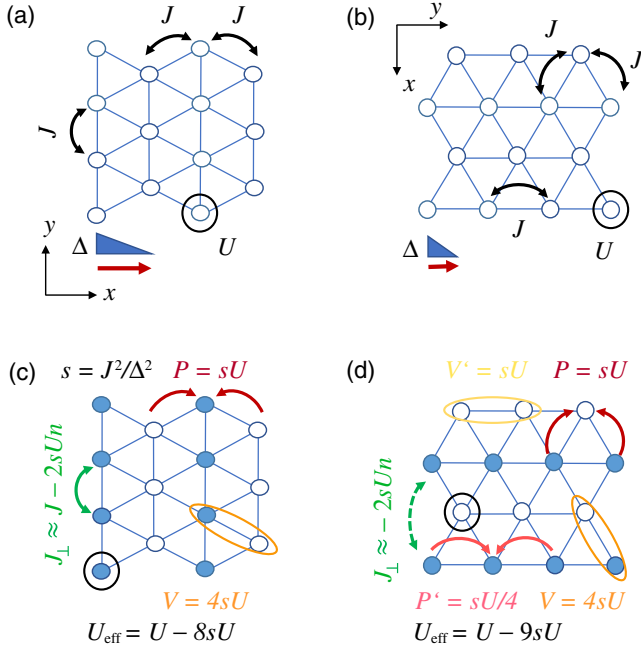


FIG. 6. Effective Hamiltonian for the tilted lattice. Visualization of the tight-binding model of the tilted lattice with energy offset  $\Delta$ , on-site interaction  $U$ , and direct hopping  $J$  (a),(b) and of the respective effective models including nearest-neighbor interactions  $V$  and pair tunneling  $P$  as well as transverse tunneling  $J_{\perp}$  and effective on-site interaction energy  $U_{\text{eff}}$  (c),(d). Compared to the usual tilt direction (a),(c), the perpendicular tilt direction (b),(d) gives rise to a smaller perpendicular hopping  $J_{\perp}$  as well as additional terms arising from resonances across two lattice sites (the primed quantities  $V'$  and  $P'$ ). The expression for the perpendicular hopping  $J_{\perp}$  in mean-field approximation contains the mean on-site occupation  $n$ .

$$\hat{H}_{\parallel, \text{eff}} = \hat{H}'_{U, \text{eff}} + \hat{H}'_P + \hat{H}'_{J_{\perp}} + \hat{H}'_{2\Delta}, \quad (\text{B16})$$

with

$$\hat{H}'_{U, \text{eff}} = \left( \frac{U}{2} - \frac{9}{2}sU \right) \sum_j \hat{n}_j (\hat{n}_j - 1) + 4sU \sum_{\langle jk \rangle_x} \hat{n}_j \hat{n}_k, \quad (\text{B17})$$

$$\hat{H}'_P = -sU \sum_{\langle jkl \rangle_x} \left( \hat{b}_j^{\dagger} \hat{b}_j^{\dagger} \hat{b}_k \hat{b}_l + \hat{b}_l^{\dagger} \hat{b}_k^{\dagger} \hat{b}_j \hat{b}_j \right), \quad (\text{B18})$$

$$\begin{aligned} \hat{H}'_{J_{\perp}} = & -sU \sum_{\langle jklm \rangle_{\diamond}} \left( \hat{b}_j^{\dagger} \hat{n}_j \hat{b}_l + \hat{b}_j^{\dagger} \hat{n}_l \hat{b}_j \right. \\ & \left. - 2\hat{b}_j^{\dagger} \hat{n}_k \hat{b}_l - 2\hat{b}_j^{\dagger} \hat{n}_m \hat{b}_l + \text{H.c.} \right), \end{aligned} \quad (\text{B19})$$

$$\hat{H}'_{2\Delta} = sU \sum_{\langle jk \rangle_y} \hat{n}_j \hat{n}_k - \frac{1}{4}sU \sum_{\langle jkl \rangle_y} \left( \hat{b}_j^{\dagger} \hat{b}_j^{\dagger} \hat{b}_k \hat{b}_l + \hat{b}_l^{\dagger} \hat{b}_k^{\dagger} \hat{b}_j \hat{b}_j \right), \quad (\text{B20})$$

where  $s = J^2/\Delta^2$  has the same form as before.  $\langle jk \rangle_x$  are nearest neighbors in  $x$  direction. Because of the geometry of the lattice these have an energy difference of  $\Delta$ .  $\langle jkl \rangle_x$  are

pairs of bonds with one bond up and one down the tilt and  $\langle jklm \rangle_{\diamond}$  denotes diamond-shaped plaquettes such that sites  $j$  and  $l$  are at the same tilt energy.  $\langle jk \rangle_y$  are nearest neighbors in  $y$  direction and  $\langle jkl \rangle_y$  are pairs of bonds in  $y$  direction. The interaction rescales as  $U \rightarrow U - 9sU$ . Effective single-particle hopping perpendicular to the tilt is present with strength  $J_{\perp} = -2sUn$ , where  $n$  is the mean-field density. In this case the hopping is to next nearest neighbors.

## 2. Motivation for density-wave formation due to pair tunneling

We motivate why the pair tunneling terms lead to the formation of the density wave by analyzing a simple 1D lattice model. We consider all states that are connected to an initial homogeneous situation consisting of an  $N$ -atom Fock state on each tube by application of  $N_{\text{steps}}$  pair tunneling events. We find that these states have a tendency to feature period 2 density modulations, as intuitively expected from the structure of the correlated pair tunneling processes. The quantitative analysis of the density correlation function averaged over all accessible states is given in Fig. 7 and it shows the growth of the staggered correlations indicative of the density wave. The correlation at a given distance  $d$  for a particular state with occupations relative to homogeneous filling  $\delta N_i$  is computed as  $\text{cov}(d) = 1/(N_{\text{sites}} - 1) \sum_{i=1}^{N_{\text{sites}}} \delta N_i \delta N_{i+d}$ .

The correlations in this analysis have a finite exponential decay length of 1.3(2) lattice sites with a hard cutoff beyond 2 lattice sites for all  $N_{\text{steps}}$  considered. The correlations observed in the experiment have a longer decay length of 2.1(7) and 2.3(5) lattice sites (Fig. 4 of main text), because the true dynamics is not captured by considering all accessible states. In the simple analysis, we neglect the

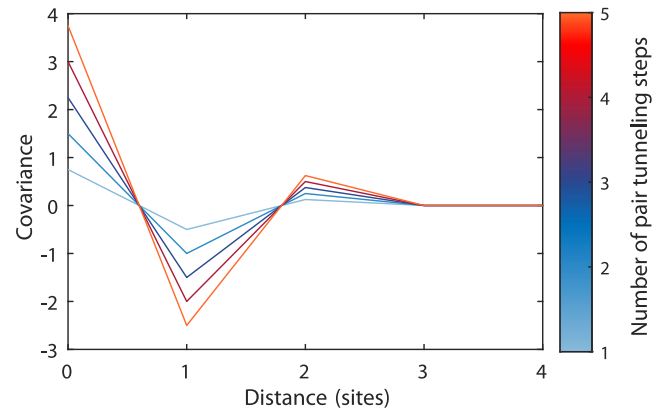


FIG. 7. Pair tunneling as mechanism for density-wave formation. The figure shows the mean covariance of all states connected to an initial homogeneous state of a system of 9 lattice sites with periodic boundary conditions with  $N_{\text{steps}}$  pair tunneling events (color coded starting from  $N_{\text{steps}} = 1$  in blue up to  $N_{\text{steps}} = 5$  in orange). The covariance shows clear staggered correlations for up to 2 lattice sites distance.

slightly different coupling strengths between the different states as well as the effect of the nearest-neighbor interactions. We also neglect coherences by starting in Fock states, which is a reasonable approximation because most coherence is rapidly lost after the quench (Appendix F). The initial atom number  $N$  per tube does not enter in the analysis, it only influences the timescale on which the pair tunneling events take place.

### 3. Explanation of $t_p$

From the pair tunneling we estimate a timescale of  $t_p = h/(16NP)$  until the maximal amplitude of the density wave, where  $P$  is the strength of the pair tunneling derived above. Compared to a standard two-level system with coupling  $\Omega$  reaching maximal transfer after  $h/(4\Omega)$ , we added an additional factor of  $4N$  here, where 4 is the number of possible pair tunneling processes in the tilted triangular lattice and  $N$  accounts for the density dependence of the process in mean field taking into account the bosonic enhancement. We expect the bosonic enhancement to be reduced due to excitations in the  $z$  direction building up after the quench, but we include the full factor  $N$  here resulting in a lower bound on the timescale.

### 4. Short-time dynamics

To understand the emergence of the density wave we consider a 1D lattice system. The initial dynamics are dominated by the fast phase rotation with frequency  $\Delta$ . The system is described by the Hamiltonian [see Eq. (B5)]:

$$\hat{\mathcal{H}} = -J \sum_j (\hat{b}_j^\dagger \hat{b}_{j+1} e^{-i\Delta t} + \hat{b}_{j+1}^\dagger \hat{b}_j e^{i\Delta t}) + \frac{U}{2} \sum_j \hat{n}_j (\hat{n}_j - 1). \quad (\text{B21})$$

To analyze the density-wave order we calculate the density-density correlation function  $\langle \hat{n}_{j_1} \hat{n}_{j_2} \rangle$ . Within a perturbative expansion, for  $\hat{O} = \hat{n}_{j_1} \hat{n}_{j_2}$  we have

$$\hat{O}(t) = \hat{O} + i \int_0^t dt_1 [\hat{\mathcal{H}}(t_1), \hat{O}] - \int_0^t dt_1 \int_0^{t_1} dt_2 [\hat{\mathcal{H}}(t_2), [\hat{\mathcal{H}}(t_1), \hat{O}]], \quad (\text{B22})$$

where we considered expansion to second order. We solve the commutators and then take the expectation value. The first-order term drops out and the second-order term has the form:

$$\langle \hat{b}_{j_1}^\dagger \hat{b}_{j_2} \hat{b}_{j_3}^\dagger \hat{b}_{j_4} \rangle \approx \frac{g(|j_1 - j_2|)g(|j_3 - j_4|)g(|j_1 - j_4|)g(|j_2 - j_3|)}{g(|j_1 - j_3|)g(|j_2 - j_4|)}. \quad (\text{B23})$$

$g(j) = \langle \hat{b}_0^\dagger \hat{b}_j \rangle \approx n_0 \exp(-|j|/r_0)$ , where  $n_0$  is the equilibrium particle number and  $r_0$  is the correlation length. We calculate the time averaged correlations  $\overline{\langle \hat{n}_{j_1} \hat{n}_{j_2} \rangle}$  by keeping the constant terms and obtain

$$\overline{\langle \hat{n}_{j_1} \hat{n}_{j_2} \rangle} = g^2(0) + sg^2(1) \left( 8F(R) - \frac{4}{F(R)} - 4F(R+1) + \frac{2}{F(R+1)} - 4F(R-1) + \frac{2}{F(R-1)} \right), \quad (\text{B24})$$

where we used  $R = a|j_1 - j_2|$  as the distance between sites with the lattice spacing  $a$  and  $s = J^2/\Delta^2$ . We define

$$F(R) = \frac{g^2(R)}{g(R+1)g(R-1)}. \quad (\text{B25})$$

We have  $F(R) = \delta_{R,0}[g^2(0)/g^2(1) - 1] + 1$  and  $1/F(R) = \delta_{R,0}[g^2(1)/g^2(0) - 1] + 1$ . In momentum space the correlations are

$$\langle \hat{\rho}_k \hat{\rho}_k \rangle = \sum_R \exp(ikR) \overline{\langle \hat{n}_{j_1} \hat{n}_{j_2} \rangle} \quad (\text{B26})$$

$$= 4sn_0^2 [1 - \cos(ka)] (2 - e^{-2a/r_0} - e^{-4a/r_0}). \quad (\text{B27})$$

This yields a density-density correlation peak at  $k = \pi/a$ , corresponding to the density pattern of period 2. The magnitude of the correlations scales with  $s$  and thus  $\Delta^2 \langle \rho_k \rho_k \rangle$  is independent of  $\Delta$ , as we describe in Fig. 3(c).

### 5. Monte Carlo simulation of the effective model

We perform Monte Carlo simulations to determine the equilibrium states of the 2D effective model for a wide range of the tilt strength. For convergence of Monte Carlo simulation, we consider a homogeneous density and a triangular lattice of size  $24 \times 24$ . We use the same  $J = h \times 13$  Hz and the same  $U/J = 0.18$  as in the experiments and the temperature  $k_B T/J = 25$ . We vary the energy offset  $\Delta$  in the range  $\Delta/J = 2-1000$  and sample the corresponding initial state via classical Metropolis Monte Carlo as in the  $c$ -field simulations. For each  $\Delta$  we carry out  $1 \times 10^6$  Monte Carlo steps per site to obtain the equilibrium state. In Fig. 8, we show the density along the  $y$  direction of the equilibrium state of a single sample. The density displays a density-wave pattern for  $\Delta$  up to a critical value of  $\Delta/J \sim 4.4$ . Above this critical value, no density wave is visible and we only observe a fluctuating density of the sample. This is in contrast to our experiments, where a density wave appears as a transient state for the tilt energies that are about 100 times larger than the effective model. Such small values of  $\Delta/J$  are hard to realize via the effective model of a tilted system, because the derivation relies on large  $\Delta/J \gg 1$ .

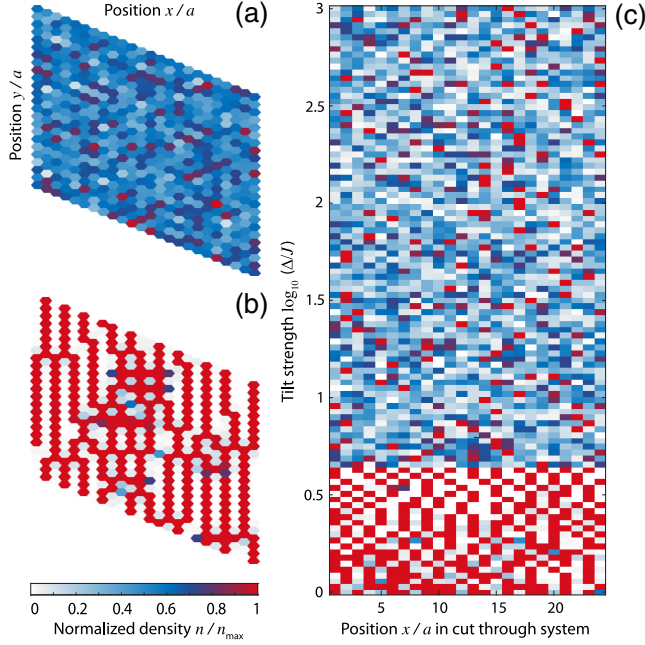


FIG. 8. Monte Carlo simulations. (a),(b) Density distributions  $n(x, y)$  of single Monte Carlo samples of the effective model for tilt energy  $\Delta$  and tunnel energy  $J$  with  $\log_{10}(\Delta/J) = 2.0$  (a) and  $\log_{10}(\Delta/J) = 0.5$  (b). The density is normalized by the maximum density  $n_{\max}$  for each image. (c) Cuts through images as in (a) and (b) as a function of  $\Delta/J$ . The density-wave pattern is visible below a critical value of  $\Delta/J \sim 4.4$ , and above this critical tilt the density is randomly fluctuating.

## APPENDIX C: EXPERIMENTAL SETUP AND METHODS

### 1. Optical lattice setup

Our optical triangular lattice setup consists of three linearly polarized running waves [42,43] of wave vector  $\mathbf{k}_i$  with  $|\mathbf{k}_i| = 2\pi/\lambda$  intersecting under an angle of  $120^\circ$ . The resulting potential can be written as

$$V_{\text{lat}2\text{D}}(\mathbf{r}) = -2V_{\text{lat}} \sum_{i>j} \cos[(\mathbf{k}_i - \mathbf{k}_j)\mathbf{r}], \quad (\text{C1})$$

where the lattice depth  $V_{\text{lat}}$  is proportional to the intensity of the lattice beams. We neglected the phases of the beams with respect to each other because they only result in a global shift of the lattice.

### 2. Site-resolved imaging

We use the technique introduced in Ref. [11] to magnify the density distributions prior to imaging. We freeze the density distribution in a deep lattice of  $V_{\text{lat}} \sim 6E_r$ , with  $E_r = \hbar^2/(2m\lambda^2)$ ,  $m = 87$  u being the mass of  $^{87}\text{Rb}$ , resulting in a tunnel coupling of  $J \sim \hbar \times 10^{-3}$  Hz. This allows us to ramp to a magnetic confinement of  $\omega_{\text{pulse}} \sim 2\pi \times 300$  Hz, which in combination with a

subsequent time of flight  $t_{\text{TOF}} \sim 20$  ms yields typical matter-wave magnification of  $\sim 40$ . We extract the on-site populations by fitting a triangular lattice to the data and subsequently summing over the Wigner-Seitz cells around the individual sites. For the images with tilt, we shift back the magnetic trap center for the matter-wave magnification, in order to reduce anharmonic matter-wave aberrations.

### 3. Parameter calibration

We calibrate the lattice depth  $V_{\text{lat}}$  via Kapitza-Dirac scattering and determine the corresponding tunneling element  $J$  via a band structure calculation. The atom loss rate is determined to be  $\gamma = [2.3(2), 2.9(2), 3.6(2)] \text{ s}^{-1}$  for energy offsets  $\Delta = \hbar \times (1.1, 1.4, 1.7)$  kHz from an exponential fit to the first 100 ms of the experiment. Note that the atom loss measures the number of atoms that get lost from the slope, thus it includes atoms that fall to the trap center, which is the reason for the tilt dependence. The experiments are performed with  $^{87}\text{Rb}$  atoms in the  $F = 2$ ,  $m_F = 2$  state in a Ioffe-Pritchard-type magnetic trap with a coil winding pattern in between a cloverleaf and a 4D configuration and with trapping frequencies  $\omega_{x,y} = 2\pi \times 135$  Hz in plane calibrated via an oscillation and  $\omega_z = 2\pi \times 30$  Hz transversally, in the latter direction dominated by the optical lattice beams. The tilt is produced by shifting the position of the magnetic trap using additional magnetic field coils. We determine the tilt from the measured shift distance of typically  $d = 15 \mu\text{m}$  and cross-check with the period of Bloch oscillations induced by the tilt. The variation of the tilt over 10 lattice sites resulting from the unchanged harmonic confinement is around  $\pm 20\%$  and is also included in the  $c$ -field simulation by modeling the full trap.

## APPENDIX D: DATA EVALUATION METHODS

### 1. Residue computation

To compute the residues  $\delta N_{jk}^{(i)}$  at site  $(j, k)$  we proceed for every single shot  $i$  in the following way. We average all images corresponding to the same experimental parameters and read out the lattice site populations of this mean image with the same masks as the ones used for the shot we want to compute the residues of. The masks of different shots differ by the phase of the optical lattice (Appendix E). The resulting populations are used as reference and are subtracted from the on-site populations of the single shot.

### 2. Correlation computation

The first step in the evaluation is to compute the covariance  $\text{cov}_{jkj'k'} = 1/(N-1) \sum_{i=1}^N \delta N_{jk}^{(i)} \delta N_{j'k'}^{(i)}$  of the residues. This is done for every site within 3 sites of the center with respect to every other site satisfying the same condition. Subsequently, the covariance is averaged for pairs of points having the same or exactly opposite

distance vector and is eventually normalized to the mean maximal tube population for the corresponding parameters. The error of the covariance is computed as  $1/\sqrt{N} \sqrt{\sum_{i=1}^N (\text{cov}_{jkj'k'}^{(i)} - \text{cov}_{jkj'k'})^2}$ , where  $\text{cov}_{jkj'k'}^{(i)} = \delta N_{jk}^{(i)} \delta N_{j'k'}^{(i)}$ . This error is then propagated when computing the mean.

### 3. Heuristic description of correlation functions

The staggered density correlation functions along the tilt are fitted with a staggered exponential decay  $c_i = c_0(-1)^i \exp(-i/L_{\parallel})$ , with an amplitude  $c_0$  and the correlation length  $L_{\parallel}$  as free parameters. For the case of weak transverse tunneling we have added a small background Gaussian function to account for an artifact from slight displacements of the clouds between measurements. The monotonic density correlation functions perpendicular to the tilt are fitted with an exponential  $c_i = c_0 \exp(-i/L_{\perp})$  for the case of weak transverse tunneling, and with a Gaussian  $c_i = c_0 \exp(-i^2/L_{\parallel}^2)$  for the case of strong transverse tunneling.

## APPENDIX E: FURTHER ANALYSIS OF EXPERIMENTAL DATA

### 1. Postselection of lattice-phase drifts

The lattice phase, i.e., the exact position of the optical lattice below a lattice site relative to the initial cloud center, is stable during one experimental preparation, but random between different experimental images. The high-resolution imaging allows us to read out this phase and to postselect on it [11]. For the investigation of the spontaneous symmetry breaking, it is important to verify that the apparently random position of the density wave is not simply triggered by this lattice phase. To do so, we repeat the analysis of the domains in Fig. 2(c) after postselection on the lattice phase and present

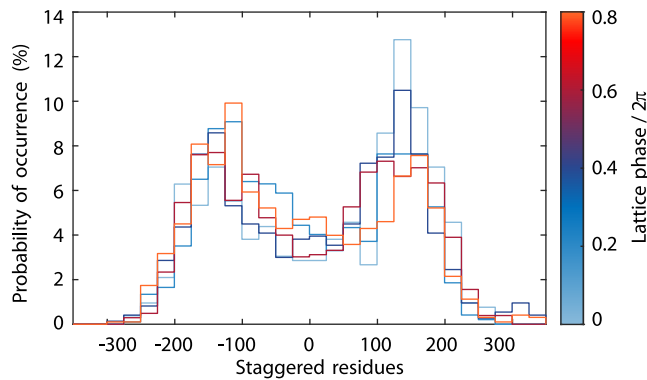


FIG. 9. Lattice-phase resolved histogram. The histogram of local density-wave order of Fig. 2(c) with separate analysis for the different lattice phases (color coded) still shows the double-peak structure reflecting the spontaneous symmetry breaking.

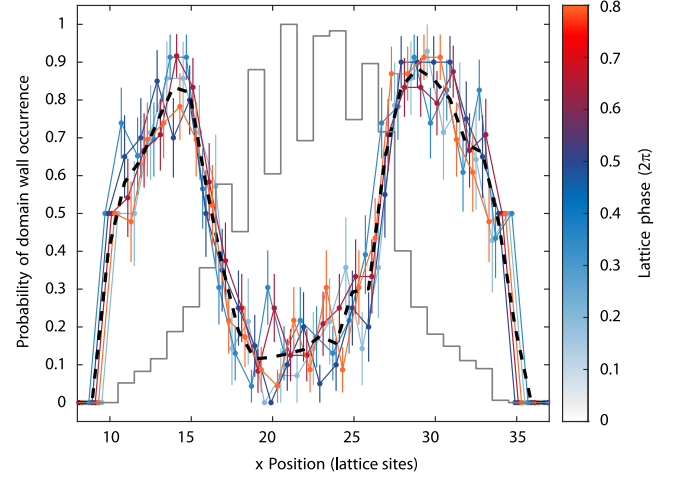


FIG. 10. Spatial distribution of the domain walls. Spatially resolved analysis of the data of Fig. 2. The curves show the probability of finding a domain wall at a given position in the cloud after integrating along the direction of the stripes. The color denotes the postselected phase of the lattice and the dashed line is the average over all data. The probability is almost homogeneous in the central region (example density shown by black curve) and trivially increases at the edge of the cloud where the density-wave pattern vanishes. The error bars denote the standard deviation of the mean.

lattice-phase resolved histograms in Fig. 9. While the statistics of the individual histograms is less extensive now, one can still recognize the double-peak structure in all histograms, which confirms that the symmetry

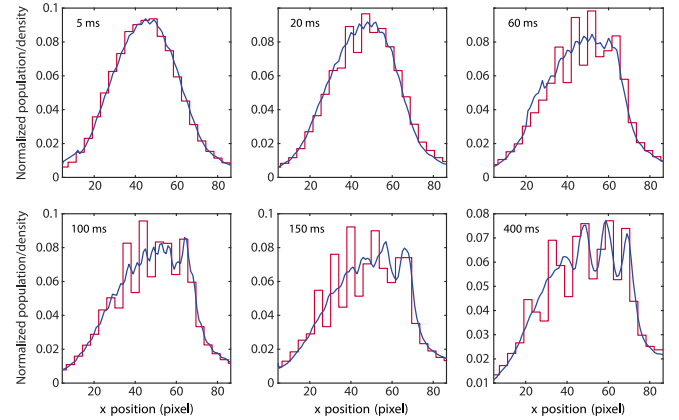


FIG. 11. Spontaneous symmetry breaking and pinning. Long-term dynamics of the density waves illustrated by the populations integrated along the columns. Exemplary single-shot profiles (red line) show the density-wave formation while the absence of a density wave in the average profile (blue line) for early times confirms the spontaneous nature of the symmetry breaking. The average profile is continuous due to the varying lattice phases of the individual images. For later times, the average profile develops density waves as well, indicating the onset of pinning, which we attribute to self-trapping.

breaking of the density wave is spontaneous and not triggered by the random lattice phase.

### 2. Spatial distribution of the domain walls

To further confirm the spontaneous nature of the symmetry breaking, we analyze the spatial distribution of the domain walls (Fig. 10). To do so we integrate the staggered residues (see Fig. 2) along the  $y$  direction, assuming no domain walls being present in this direction. For each shot we track the sign changes which we interpret as domain walls. Subsequently, for every position, we divide the number of domain walls that we obtain by the number of shots with the same parameters to compute a local probability.

We find that this probability is almost homogeneous across the relevant region of significant density-wave pattern, as expected for spontaneous symmetry breaking, with a value around 10%–20%. There is, however, a slight

increase in the number of domain walls at the outer part of the cloud in the direction of the trap center, which might be due to the atoms slowly falling down the slope. Outside this relevant region of about 10 lattice sites containing clear density waves, the signal sharply rises reflecting the absence of the pattern, which makes domain walls ill defined. In this outer region, the analysis is more sensitive to systematic effects arising, e.g., from the density envelope, and therefore does not exactly yield the probability of 0.5 expected for uncorrelated fluctuations.

### 3. Pinning of the density-wave pattern for long hold times

For longer hold times (Fig. 11), we find an intriguing interplay of pair tunneling and single-particle tunneling: the average profile develops density waves as well, which we attribute to steep density gradients formed due to self-trapping [44]. This pins the density wave at a fixed position

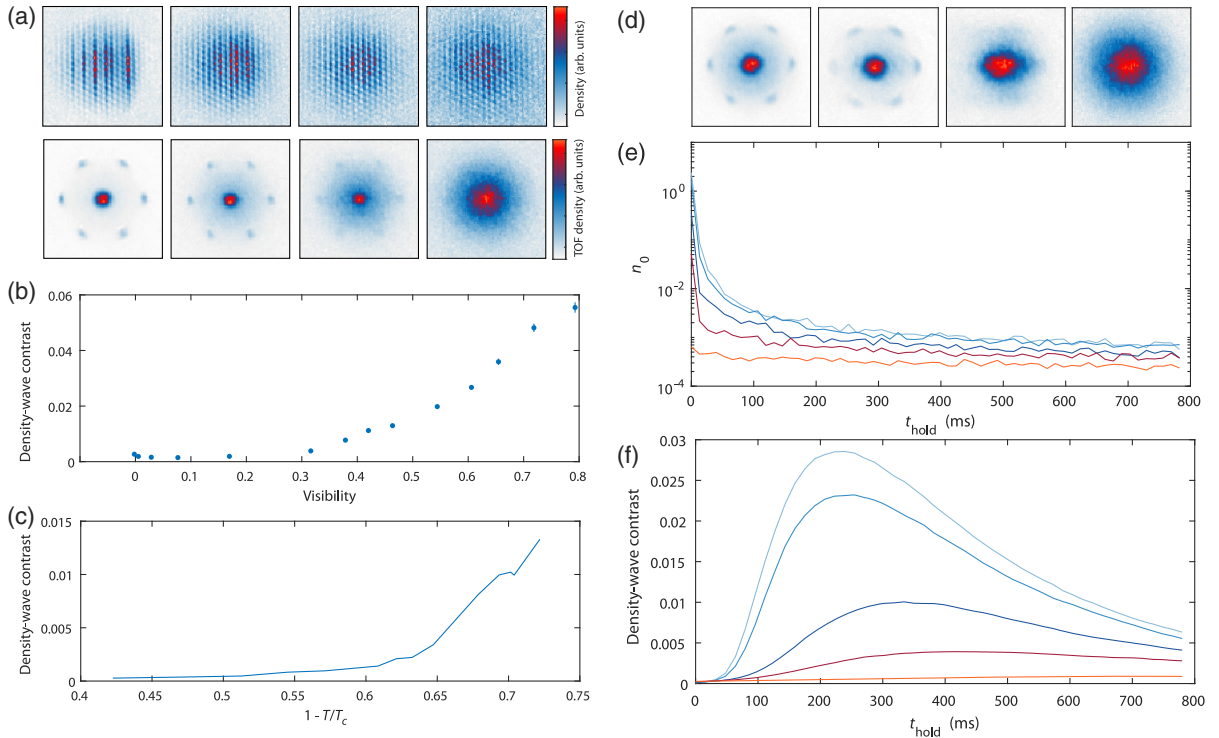


FIG. 12. Influence of coherence on the density-wave formation. (a) Density-wave pattern for different initial temperatures of the BEC before the quench into the tilted system (upper row). The coherence of the initial system is evidenced by the visibility of the Bragg peaks in a time-of-flight (TOF) measurement before the quench (lower row). The temperature is increased deliberately by a hold time in the lattice of (from left to right) (0.1, 750, 1200, 1800) ms leading to a visibility of (0.79, 0.42, 0.17, 0.006). (b) Density-wave order as a function of the Bragg-peak visibility in the experiment for a hold time of 100 ms and an energy offset of  $\Delta = \hbar \times 1.4$  kHz. All error bars correspond to the 68% confidence interval. (c) Simulation of the density-wave order for the experimental parameters, plotted as a function of  $1 - T/T_c$ , where  $T_c$  is the critical temperature of a noninteracting gas. (d) TOF measurements for (0.1, 1.1, 2.1, 1200) ms (from left to right) hold time after the quench and  $\Delta = \hbar \times 1.1$  kHz. The hold times are approximately stroboscopic with respect to the Bloch oscillation period. (e) The condensate density  $n_0$  versus time in the numerical simulation for different temperatures reproduces the rapid loss of coherence and shows that a very small coherent fraction remains, which is not experimentally detectable. (f) The density-wave order for the parameters in (e) shows that this residual coherence is crucial for the density-wave formation. The different colors stand for different initial temperatures of  $T/T_c = 0.28, 0.32, 0.39, 0.45,$  and  $0.53$  (top to bottom).

making the symmetry breaking not spontaneous anymore. We observe experimentally an inward propagation of the pinning, starting from the edge at the lower end of the slope. This behavior seems reminiscent of the spontaneous formation and later stabilization also observed for super-solid droplets in continuous systems [45].

## APPENDIX F: ADDITIONAL MEASUREMENTS

### 1. Influence of coherence

We study the importance of coherence for the formation of the density-wave order. As a first point, we compare the density-wave order for different initial temperatures before the quench into the tilted system and find that the density-wave order vanishes when no initial coherence is present [see Figs. 12(a)–12(c)].

As a second point, we investigate the coherence after the quench and find that while most coherence is rapidly lost after a few Bloch oscillation periods [Fig. 12(d)], a residual coherence is detectable in the simulation results and the density-wave formation vanishes as a function of temperature together with this residual coherence [Figs. 12(e) and 12(f)]. The simulated condensate density  $n_0$ , which is a measure of the coherence between the lattice sites, is determined by averaging the complex field  $\psi_i$  within a central region with a radius of 6 sites and then averaging the absolute value squared over the thermal ensemble, i.e.,  $n_0 = \langle |1/N_r \sum_i \psi_i|^2 \rangle_{\text{ensemble}}$ , with  $N_r$  being the number of sites in the region of interest. The data in Fig. 12(d) are for the tilt perpendicular to a lattice vector, where the residual coherence also shows in the experimental data as a small anisotropy of the time-of-flight distribution. For the other tilt direction with the much smaller tunneling along the columns, the coherence is smaller and we do not observe an anisotropy in the time-of-flight images. Because of the small coherent fraction, our density wave would not be visible as a second Bragg peak in time-of-flight measurements as in Refs. [14–16] and therefore explicitly requires the novel microscopy technique of Ref. [11].

### 2. Confirmation of the interaction-driven dynamics

In Fig. 3, we have observed the interaction-driven nature of the density-wave formation via the slowing-down of the long-time dynamics due to atom losses. Here, we further strengthen this point, by studying the formation dynamics of the density wave for different initial atom numbers (Fig. 13). Indeed, we find much faster buildup of the density-wave order with increasing atom number both in the experiment and the numerical simulation.

The atom-number dependence of the density-wave build-up time is consistent with the atom-number dependence of the pair tunneling time, which drives the formation. Furthermore, also the atom-number dependence of the maximal contrast of the density wave can be attributed

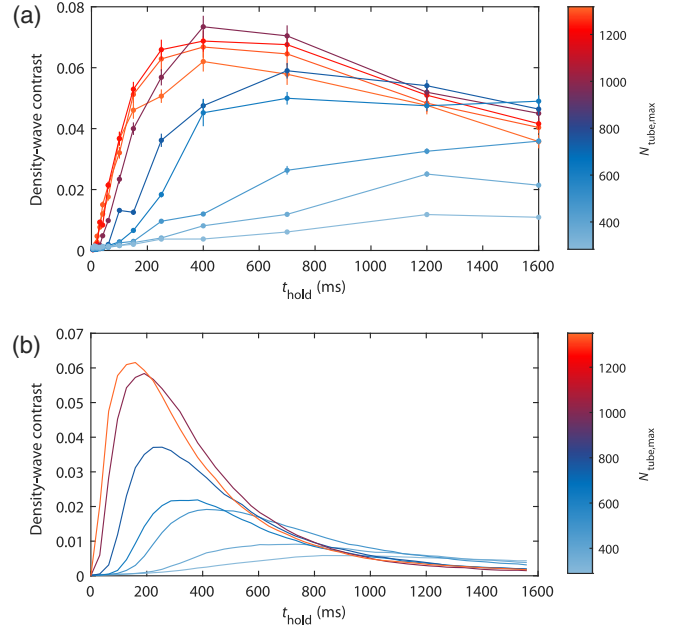


FIG. 13. Atom-number dependence. (a) Experimental density-wave order dynamics as a function of the initial atom number (color coded using the biggest tube population at  $t \sim 0$ ). The energy offset was  $\Delta = h \times 1.4$  kHz. All error bars correspond to the 68% confidence interval. (b) Simulation for the corresponding parameters and  $k_B T/J = 100$ , without including atom loss.

to this atom-number dependence of the density-wave build-up time, which is competing with the slow single-particle tunneling.

### 3. Incommensurate tilt directions

We also study incommensurate tilt directions, which are not along or perpendicular to a direct lattice vector, by shifting the magnetic trap in the appropriate directions. The dynamics for a tilt direction  $10^\circ$  rotated against the direction perpendicular to a direct lattice vector is shown in Fig. 14. Because the tilt is produced by the shifted magnetic trap, its direction changes with position. The force from the tilt can be decomposed into a component perpendicular to a lattice vector, where the atoms are Stark localized, and a component along a lattice vector, where the atoms can move. Indeed, a fraction of the atoms moves along the latter direction. For the given geometry, the component along the lattice vector vanishes after the atoms have moved by about 5 lattice sites and the motion stops there. The atoms automatically align with a commensurate tilt direction.

This splitting is reminiscent of early experiments in Josephson junction arrays finding that the superfluid fraction can move through the lattice, while the thermal fraction is pinned [46,47]. The observed separation might therefore point a way to distill the zero-temperature part of the cloud. The formation of the density wave is restricted

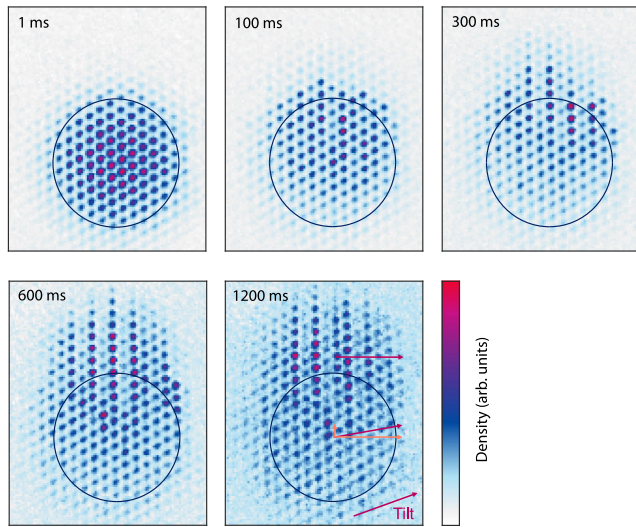


FIG. 14. Incommensurate tilt direction. Experimental images for different hold times after quenching to a tilt, which is 10 tilted against the direction perpendicular to a direct lattice vector. The red arrows indicate the local tilt direction, the orange arrows show the projection of the tilt onto a lattice vector and onto the direction perpendicular to it. A fraction of the cloud moves from the initial position (circles) to a position where the tilt is again commensurate (topmost arrow in the last panel) and forms a density wave with large contrast.

to a small region with minimal tilt along the stripe pattern and reaches a larger contrast than in the commensurate situations discussed in the main text. This is in line with the observed relevance of coherence discussed above.

[1] M. C. Cross and P. C. Hohenberg, *Pattern Formation Outside of Equilibrium*, *Rev. Mod. Phys.* **65**, 851 (1993).  
 [2] Z. Zhang, K. X. Yao, L. Feng, J. Hu, and C. Chin, *Pattern Formation in a Driven Bose-Einstein Condensate*, *Nat. Phys.* **16**, 652 (2020).  
 [3] F. Böttcher, J.-N. Schmidt, J. Hertkorn, K. S. H. Ng, S. D. Graham, M. Guo, T. Langen, and T. Pfau, *New States of Matter with Fine-Tuned Interactions: Quantum Droplets and Dipolar Supersolids*, *Rep. Prog. Phys.* **84**, 012403 (2021).  
 [4] S. Sachdev, K. Sengupta, and S. M. Girvin, *Mott Insulators in Strong Electric Fields*, *Phys. Rev. B* **66**, 075128 (2002).  
 [5] S. Pielawa, T. Kitagawa, E. Berg, and S. Sachdev, *Correlated Phases of Bosons in Tilted Frustrated Lattices*, *Phys. Rev. B* **83**, 205135 (2011).  
 [6] J. Simon, W. S. Bakr, R. Ma, M. E. Tai, P. M. Preiss, and M. Greiner, *Quantum Simulation of Antiferromagnetic Spin Chains in an Optical Lattice*, *Nature (London)* **472**, 307 (2011).  
 [7] R. Ma, M. E. Tai, P. M. Preiss, W. S. Bakr, J. Simon, and M. Greiner, *Photon-Assisted Tunneling in a Biased Strongly Correlated Bose Gas*, *Phys. Rev. Lett.* **107**, 095301 (2011).  
 [8] F. Meinert, M. J. Mark, E. Kirilov, K. Lauber, P. Weinmann, M. Gröbner, A. J. Daley, and H. C. Nägerl, *Observation of*

*Many-Body Dynamics in Long-Range Tunneling after a Quantum Quench*, *Science* **344**, 1259 (2014).  
 [9] H. Bernien, S. Schwartz, A. Keesling, H. Levine, A. Omran, H. Pichler, S. Choi, A. S. Zibrov, M. Endres, M. Greiner, V. Vuletic, and M. D. Lukin, *Probing Many-Body Dynamics on a 51-Atom Quantum Simulator*, *Nature (London)* **551**, 579 (2017).  
 [10] O. Dutta, M. Gajda, P. Hauke, M. Lewenstein, D. S. Lühmann, B. A. Malomed, T. Sowiński, and J. Zakrzewski, *Non-Standard Hubbard Models in Optical Lattices: A Review*, *Rep. Prog. Phys.* **78** (2015).  
 [11] L. Asteria, H. P. Zahn, M. N. Kosch, K. Sengstock, and C. Weitenberg, *Quantum Gas Magnifier for Sub-Lattice-Resolved Imaging of Three-Dimensional Quantum Systems*, *Nature (London)* **599**, 571 (2021).  
 [12] E. Guardado-Sanchez, A. Morningstar, B. M. Spar, P. T. Brown, D. A. Huse, and W. S. Bakr, *Subdiffusion and Heat Transport in a Tilted Two-Dimensional Fermi-Hubbard System*, *Phys. Rev. X* **10**, 011042 (2020).  
 [13] S. Scherg, T. Kohler, P. Sala, F. Pollmann, B. H. Madhusudhana, I. Bloch, and M. Aidelsburger, *Observing Non-Ergodicity due to Kinetic Constraints in Tilted Fermi-Hubbard Chains*, *Nat. Commun.* **12**, 4490 (2021).  
 [14] L. Fallani, L. De Sarlo, J. E. Lye, M. Modugno, R. Saers, C. Fort, and M. Inguscio, *Observation of Dynamical Instability for a Bose-Einstein Condensate in a Moving 1D Optical Lattice*, *Phys. Rev. Lett.* **93**, 140406 (2004).  
 [15] M. Cristiani, O. Morsch, N. Malossi, M. Jona-Lasinio, M. Anderlini, E. Courtade, and E. Arimondo, *Instabilities of a Bose-Einstein Condensate in a Periodic Potential: An Experimental Investigation*, *Opt. Express* **12**, 4 (2004).  
 [16] N. Gemelke, E. Sarajlic, Y. Bidel, S. Hong, and S. Chu, *Parametric Amplification of Matter Waves in Periodically Translated Optical Lattices*, *Phys. Rev. Lett.* **95**, 170404 (2005).  
 [17] M. Schulz, C. A. Hooley, R. Moessner, and F. Pollmann, *Stark Many-Body Localization*, *Phys. Rev. Lett.* **122**, 040606 (2019).  
 [18] A. Cao, R. Sajjad, E. Q. Simmons, C. J. Fujiwara, T. Shimasaki, and D. M. Weld, *Transport Controlled by Poincaré Orbit Topology in a Driven Inhomogeneous Lattice Gas*, *Phys. Rev. Research* **2**, 032032(R) (2020).  
 [19] S. Burger, F. S. Cataliotti, C. Fort, F. Minardi, M. Inguscio, M. L. Chiofalo, and M. P. Tosi, *Superfluid and Dissipative Dynamics of a Bose-Einstein Condensate in a Periodic Optical Potential*, *Phys. Rev. Lett.* **86**, 4447 (2001).  
 [20] N. D. Oppong, G. Pasqualetti, O. Bettermann, P. Zechmann, M. Knap, I. Bloch, and S. Fölling, *Probing Transport and Slow Relaxation in the Mass-Imbalanced Fermi-Hubbard Model*, *arXiv:2011.12411*.  
 [21] M. Ueda, *Quantum Equilibration, Thermalization and Prethermalization in Ultracold Atoms*, *Nat. Rev. Phys.* **2**, 669 (2020).  
 [22] D.-S. Lühmann, *Twisted Superfluid Phase in the Extended One-Dimensional Bose-Hubbard Model*, *Phys. Rev. A* **94**, 011603(R) (2016).  
 [23] J. Struck, M. Weinberg, C. Ölschläger, P. Windpassinger, J. Simonet, K. Sengstock, R. Höppner, P. Hauke, A. Eckardt, M. Lewenstein, and L. Mathey, *Engineering Ising-XY*

- Spin-Models in a Triangular Lattice Using Tunable Artificial Gauge Fields*, *Nat. Phys.* **9**, 738 (2013).
- [24] C. V. Parker, L. C. Ha, and C. Chin, *Direct Observation of Effective Ferromagnetic Domains of Cold Atoms in a Shaken Optical Lattice*, *Nat. Phys.* **9**, 769 (2013).
- [25] T. Kock, M. Ölschläger, A. Ewerbeck, W.-M. Huang, L. Mathey, and A. Hemmerich, *Observing Chiral Superfluid Order by Matter-Wave Interference*, *Phys. Rev. Lett.* **114**, 115301 (2015).
- [26] S. Baier, M. J. Mark, D. Petter, K. Aikawa, L. Chomaz, Z. Cai, M. Baranov, P. Zoller, and F. Ferlaino, *Extended Bose-Hubbard Models with Ultracold Magnetic Atoms*, *Science* **352**, 201 (2016).
- [27] F. Meinert, M. J. Mark, K. Lauber, A. J. Daley, and H.-C. Nägerl, *Floquet Engineering of Correlated Tunneling in the Bose-Hubbard Model with Ultracold Atoms*, *Phys. Rev. Lett.* **116**, 205301 (2016).
- [28] I. Dimitrova, N. Jepsen, A. Buyskikh, A. Venegas-Gomez, J. Amato-Grill, A. Daley, and W. Ketterle, *Enhanced Superexchange in a Tilted Mott Insulator*, *Phys. Rev. Lett.* **124**, 043204 (2020).
- [29] A. Bohrdt, L. Homeier, I. Bloch, E. Demler, and F. Grusdt, *Strong Pairing in Mixed Dimensional Bilayer Antiferromagnetic Mott Insulators*, [arXiv:2108.04118](https://arxiv.org/abs/2108.04118).
- [30] G. Zisling, D. M. Kennes, and Y. B. Lev, *Transport in Stark Many Body Localized Systems*, [arXiv:2109.06196](https://arxiv.org/abs/2109.06196).
- [31] C. Weitenberg and J. Simonet, *Tailoring Quantum Gases by Floquet Engineering*, *Nat. Phys.* **17**, 1342 (2021).
- [32] S. Rachel, *Interacting Topological Insulators: A Review*, *Rep. Prog. Phys.* **81**, 116501 (2018).
- [33] M. Jamotte, N. Goldman, and M. Di Liberto, *Strain and Pseudo-Magnetic Fields in Optical Lattices from Density-Assisted Tunneling*, *Commun. Phys.* **5**, 30 (2022).
- [34] S. Mukherjee and M. C. Rechtsman, *Observation of Floquet Solitons in a Topological Bandgap*, *Science* **368**, 856 (2020).
- [35] A. Kshetrimayum, J. Eisert, and D. M. Kennes, *Stark Time Crystals: Symmetry Breaking in Space and Time*, *Phys. Rev. B* **102**, 195116 (2020).
- [36] V. P. Singh, W. Weimer, K. Morgener, J. Siegl, K. Hueck, N. Luick, H. Moritz, and L. Mathey, *Probing Superfluidity of Bose-Einstein Condensates via Laser Stirring*, *Phys. Rev. A* **93**, 023634 (2016).
- [37] C. Mora and Y. Castin, *Extension of Bogoliubov Theory to Quasicondensates*, *Phys. Rev. A* **67**, 053615 (2003).
- [38] W. Magnus, *On the Exponential Solution of Differential Equations for a Linear Operator*, *Commun. Pure Appl. Math.* **7**, 649 (1954).
- [39] S. Blanes, F. Casas, J. Oteo, and J. Ros, *The Magnus Expansion and Some of Its Applications*, *Phys. Rep.* **470**, 151 (2009).
- [40] B. Zhu, T. Rexin, and L. Mathey, *Magnus Expansion Approach to Parametric Oscillator Systems in a Thermal Bath*, *Z. Naturforsch. A* **71**, 921 (2016).
- [41] O. Jürgensen, K. Sengstock, and D.-S. Lühmann, *Density-Induced Processes in Quantum Gas Mixtures in Optical Lattices*, *Phys. Rev. A* **86**, 043623 (2012).
- [42] C. Becker, P. Soltan-Panahi, J. Kronjäger, S. Dörscher, K. Bongs, and K. Sengstock, *Ultracold Quantum Gases in Triangular Optical Lattices*, *New J. Phys.* **12**, 065025 (2010).
- [43] N. Fläschner, B. S. Rem, M. Tarnowski, D. Vogel, D.-S. Lühmann, K. Sengstock, and C. Weitenberg, *Experimental Reconstruction of the Berry Curvature in a Floquet Bloch Band*, *Science* **352**, 1091 (2016).
- [44] T. Anker, M. Albiez, R. Gati, S. Hunsmann, B. Eiermann, A. Trombettoni, and M. K. Oberthaler, *Nonlinear Self-Trapping of Matter Waves in Periodic Potentials*, *Phys. Rev. Lett.* **94**, 020403 (2005).
- [45] M. Sohmen, C. Politi, L. Klaus, L. Chomaz, M. J. Mark, M. A. Norcia, and F. Ferlaino, *Birth, Life, and Death of a Dipolar Supersolid*, *Phys. Rev. Lett.* **126**, 233401 (2021).
- [46] F. S. Cataliotti, S. Burger, C. Fort, P. Maddaloni, F. Minardi, A. Trombettoni, A. Smerzi, and M. Inguscio, *Josephson Junction Arrays with Bose-Einstein Condensates*, *Science* **293**, 843 (2001).
- [47] F. S. Cataliotti, L. Fallani, F. Ferlaino, C. Fort, P. Maddaloni, and M. Inguscio, *Superfluid Current Disruption in a Chain of Weakly Coupled Bose-Einstein Condensates*, *New J. Phys.* **5**, 71 (2003).